

RESEARCH ARTICLE | AUGUST 03 2023

Dependence of ion charge-energy emission from Nd:YAG-laser-produced plasma on laser intensity in the $0.4\text{--}40 \times 10^{10} \text{ W/cm}^2$ range

Special Collection: [Plasma Sources for Advanced Semiconductor Applications](#)

Lucas Poirier ; Adam Lassise; Ronnie Hoekstra ; John Sheil ; Oscar O. Versolato  

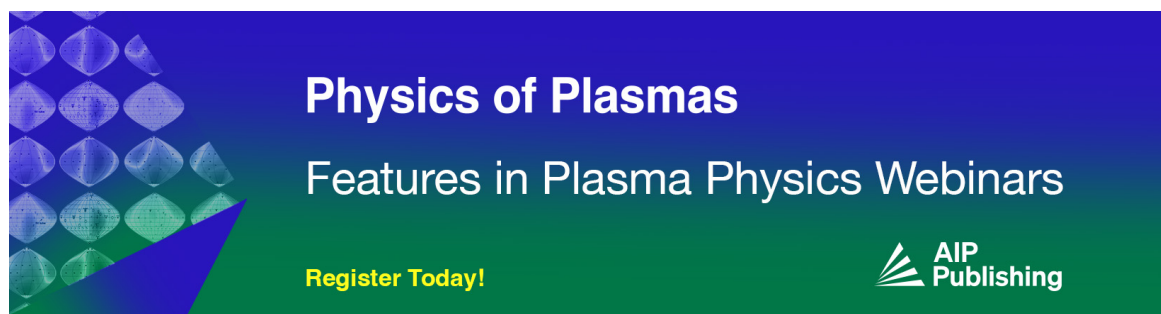


Phys. Plasmas 30, 083505 (2023)

<https://doi.org/10.1063/5.0150883>




CrossMark



Physics of Plasmas
Features in Plasma Physics Webinars

Register Today!



Dependence of ion charge-energy emission from Nd:YAG-laser-produced plasma on laser intensity in the $0.4\text{--}40 \times 10^{10} \text{ W/cm}^2$ range

Cite as: Phys. Plasmas **30**, 083505 (2023); doi: 10.1063/5.0150883

Submitted: 16 March 2023 · Accepted: 6 July 2023 ·

Published Online: 3 August 2023



View Online



Export Citation



CrossMark

Lucas Poirier,^{1,2}  Adam Lassise,¹ Ronnie Hoekstra,^{1,3}  John Sheil,^{1,2}  and Oscar O. Versolato^{1,2,a)} 

AFFILIATIONS

¹Advanced Research Center for Nanolithography, Science Park 106, Amsterdam 1098 XC, The Netherlands

²Department of Physics and Astronomy, and LaserLaB, Vrije Universiteit Amsterdam, De Boelelaan 1081, Amsterdam 1081 HV, The Netherlands

³Zernike Institute for Advanced Materials, University of Groningen, Nijenborgh 4, Groningen 9747 AG, The Netherlands

Note: This paper is part of the Special Topic: Plasma Sources for Advanced Semiconductor Applications.

^{a)} Author to whom correspondence should be addressed: o.versolato@arcnl.nl

ABSTRACT

We experimentally characterize the ionic emission, including the individual charge states Sn^{z+} ($z = 1, \dots, 8$), from laser-produced tin plasma as a function of the intensity of the employed ns-pulsed laser. The plasma is generated in a vacuum from tin microdroplets (diameter ranging from 17 to 35 μm) using pulsed Nd:YAG laser light (laser wavelength $\lambda = 1.064 \mu\text{m}$) over a range of intensities ($0.4\text{--}40 \times 10^{10} \text{ W/cm}^2$). We measure charge-state-resolved and integrated ion energy distributions at seven angular positions around the plasma using seven retarding field analyzers. We highlight peak features in both types of spectra and describe the dependence of their energies on laser intensity with power-law functions. The resulting power laws match those derived from plasma radiation hydrodynamics theory. The analytical scaling laws exhibit strong isotropy, while the ion energy spectra are highly anisotropic.

© 2023 Author(s). All article content, except where otherwise noted, is licensed under a Creative Commons Attribution (CC BY) license (<http://creativecommons.org/licenses/by/4.0/>). <https://doi.org/10.1063/5.0150883>

I. INTRODUCTION

Extreme ultraviolet (EUV) light is utilized in the lithographic process to produce nanometer-sized features on silicon chips. Industrially, tin laser-produced plasmas (LPP) are used to produce 13.5 nm EUV light. The density, temperature, and morphology of the LPP are optimized for EUV production. However, ion emission from the LPP is also to be considered, as this adverse process is known to take a toll on EUV output from the source, e.g., by gradually tarnishing the performance of the surrounding EUV transport optics, for instance, by implantation and sputtering on their surface. Furthermore, all the laser energy transferred to ion kinetics is not available for EUV production and can therefore be considered to be wasted. One parameter of particular interest is the intensity of the laser pulses, where a higher intensity is associated with the generation of more ions with higher kinetic energies, which at some point may be no longer stopped by the buffer gases that are typically employed in industrial sources of EUV light to mitigate the impact of ion “debris.”

The parameter space of the LPP experiment is vast (drive laser wavelength, laser pulse morphology and intensity, target volume and morphology, single- or multi-laser-pulse schemes, etc.), and currently, systematic exploration is incomplete. Analytical work has produced valuable general insights into plasma expansion.^{1–3} However, analytical work necessarily relies on highly idealized and simplified conditions and needs to be supported by dedicated numerical simulations and experiments. Existing experimental research examines the energy, charge state, and angular distributions of emitted ions for experimental parameters similar to those of nanolithographic EUV sources, using a variety of ion diagnostic tools. Such tools include electrostatic probes,^{4,5} Faraday cups,^{6–8} electrostatic analyzers,^{7–11} retarding field analyzers,¹² and Thompson parabolas.⁶ Many studies observed anisotropy in the charge-integrated^{4,6,7,13–17} and charge-state-resolved ion emission into a buffer gas.⁹ Morris *et al.*,^{10,11} O'Connor *et al.*,¹⁸ and Brandstätter *et al.*⁴ studied angle- and charge-state-resolved ion emission in a solid tin target experiment. They reported increasing ion charge states and increasing average kinetic energies for decreasing

angles with respect to the direction of the incoming laser pulse. O'Connor *et al.*¹⁸ additionally measured increasing numbers of ions, average ion energies, and average charge states with increasing laser intensities. We recently combined absolute angle- and charge-state-resolved kinetic energy measurements on an industrially relevant tin-microdroplet-based plasma, expanding into the vacuum.¹⁹ More specifically, the anisotropy of the ion emission was investigated. The presence of a high-energy peak in the ion energy spectra was found to be more prominent for smaller angles with respect to the direction of the drive laser.¹⁹ Furthermore, our studies showed that the experimental ion energy spectra could be reproduced using a numerical single-fluid, single-temperature radiation hydrodynamic approach employing the code RALEF-2D.^{19,20} Given the complexity of ion flow characterization, we previously performed proof-of-principle experiments. In these experiments, we simplified our approach by (i) focusing on just a single laser intensity and, moreover, (ii) by assessing only the overall mass flow and not the individual charge states contributing to it. To complement our previous work,^{19,20} as well as that of Morris *et al.*^{10,11} and O'Connor *et al.*,¹⁸ we here investigate experimentally the dependence of ion emission, including specifically the individual charge states, on laser intensity—an important parameter for the optimization of EUV light production and for the optimization of tin usage for EUV production and suppression of ion debris. Retarding field analyzers (RFAs) are employed to provide information on ion yield, energy, and charge state. Seven RFA detectors placed around the LPP are used to map the angular dependence of the ion emission. First, we recall the experimental setup used for ion detection at ARCNL and describe the explored parameter space. We present charge-state-resolved and charge-integrated ion energy spectra, where we highlight notable spectral features. Those features and their variation with increasing laser intensity are the main targets of our investigation. We interpret our findings from the perspective of hydrodynamic plasma expansion, performing power-law fits, and compare the results to plasma radiation hydrodynamics theory.

II. EXPERIMENTAL METHODS

A. Experimental setup

The experimental setup (see Fig. 1) is thoroughly described in previous publications.^{19,21,22} Here, we briefly summarize the key experimental parameters. The laser used to drive the tin plasma is a 10 Hz pulsed Nd:YAG laser operating at 1064 nm wavelength. The laser pulses have a Gaussian profile in both temporal and spatial coordinates. The spatial full-width-at-half-maximum (FWHM_{xy}) is 100 μm (the spatial profile has cylindrical symmetry), and the temporal full-width-at-half-maximum (FWHM_t) is either 8 or 10 ns. The pulse duration is here determined by the Q-switch delay of the laser, with the shorter 8 ns pulse length enabling larger pulse energies. Tin plasmas are generated in a vacuum chamber (maintained at approximately 10⁻⁷ mbar) from liquid tin droplets having three diameters, namely, 17, 27, and 35 μm. For each droplet size, we set the total laser pulse energy to four values ranging from approximately 5 to 100 mJ for the 10 ns pulse length measurements (on 17- and 27-μm-diameter droplets), and from approximately 5 to 350 mJ for the 8 ns case (17- and 35-μm-diameter droplets). Note that the amount of laser light absorbed by the droplet and plasma not only depends on the initial size of the droplet but also on the radial expansion of the tin mass (either in the form of tin liquid or plasma) as the laser pulse is absorbed. Unless stated otherwise, the 27-μm-diameter droplets and

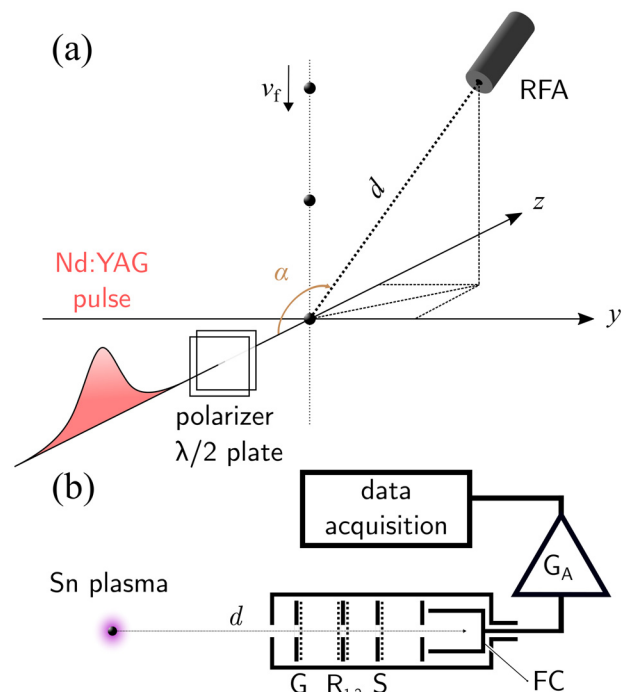


FIG. 1. Sketch of the experimental setup. (a) Droplets vertically travel with velocity v_f until they are illuminated by a Nd:YAG laser pulse. The position of an RFA is defined by its distance from the LPP (d) and the angle (α) between the direction toward the RFA and the negative z -axis along which the incoming laser pulse travels. The angle α is calculated from the elevation and the azimuth of the RFA with respect to the laser axis. A thin-film polarizer and $\lambda/2$ wave plate are used to adjust the intensity of the laser pulse. (b) The main elements of the RFA are shown; four grids (G , R_1 , R_2 , and S) are located in the path of the tin ions (Ref. 19 for further details). The ion current in the Faraday cup (FC) is amplified (denoted by G_A) and recorded by an oscilloscope. Reproduced from Poirier *et al.*, Phys. Plasmas **29**, 123102 (2022) with the permission of AIP Publishing.

10-ns FWHM_t pulses are used. For this droplet size, the set laser pulse energies in a vacuum are 8, 25, 58, and 97 mJ, corresponding to laser intensities of approximately 6, 21, 48, and 80 GW/cm². This intensity range is relevant for laser pre-pulses that are used in the industry to pre-shape tin targets²³ before interacting with a more energetic main pulse.

B. Ion diagnostics

An array of seven retarding field analyzers gives angle-resolved information on the energy and charge of the ion emission from the LPP. The devices' corresponding post-processing analysis was described in detail in previous studies.^{19,22} The post-processing “bottom-up” analysis²² constructs charge-integrated ion spectra (dN/dE or dQ/dE) through a summation and interpolation of the spectra from individual charge states as follows:

$$\frac{dN}{dE} = \sum_z \frac{dN_z}{dE}, \quad (1)$$

$$\frac{dQ}{dE} = \sum_z \frac{dQ_z}{dE} = \sum_z ze \frac{dN_z}{dE}. \quad (2)$$

The seven RFAs are placed at $\alpha = 30^\circ, 41^\circ, 64^\circ, 90^\circ, 120^\circ, 139^\circ,$ and 150° with respect to the direction of the incoming laser beam [in the current case of cylindrical symmetry, a single angle α suffices to describe the angular position of each RFA—Fig. 1(a)]. The distances from the LPP to the RFAs range from 296 to 420 mm. The distance to the LPP and the aperture size (5 mm in diameter) of the RFAs together define their solid angle of collection, for which the ion signal is corrected. The transmission of the devices is defined by that of the four-grid stack [Fig. 1(b)]. As discussed in Ref. 19, the full transmission lies between 41% and 83%, corresponding to the extreme cases of minimum and maximum mutual overlap of the grids. In the following, we take a transmission value of 62%, cf. Ref. 19. Two of the grids carry the retarding electric potential used for charge state unraveling. The purpose of each of the grids is discussed in detail in Ref. 22.

The raw RFA signal is amplified using a custom-built high-speed, large bandwidth trans-impedance amplifier with a gain of 25 kV/A.²² The ion signal reduces to the noise floor at very short (few ns) and very long (few hundred μ s) time-of-flight values, with few ions arriving. In the charge-integrated kinetic energy distribution representation, the noise level scales with $E^{-3/2}$ effectively rendering the signal to have too low signal-to-noise for energies below about 10 eV and above a few keV (the specific values depend on experimental parameters), see also Ref. 22.

III. RESULTS AND DISCUSSION

We examine the dependence of the ion energy spectra on laser intensity from tin LPPs produced from mass-limited droplet targets. Four laser intensities are set for each selected droplet diameter, ranging 0.4×10^{10} to 40×10^{10} W/cm².

A. Intensity dependence of charge-resolved ion energies

Using our post-processing scheme,²² energy distributions are retrieved for each charge state observed in the LPP.

1. Charge-resolved ion energy spectra

Figure 2 shows the variation of charge-state-resolved spectra with laser intensity at a 30° observation angle for the 27- μ m-diameter droplet target. In the following, we restrict the low-energy bound to 100 eV for the sake of visual clarity. Following Ref. 24, we calculate the laser intensity using $I = (2\sqrt{\ln 2/\pi})^3 E_L / (\text{FWHM}_x^2 \text{FWHM}_t)$, where E_L is total laser pulse energy. First, we note that the (average) kinetic energy of the ions increases with increasing charge state. Similar observations were made in our studies,^{21,22} however without any quantitative assessment, as well as in O'Connor *et al.*¹⁸ and Morris *et al.*¹¹ The former study reports a linear increase in the average ion kinetic energy with charge state.¹⁸ The increase in kinetic energy with charge state saturates around a few keV for higher charge states ($z > 5$ for the measurement presented in Fig. 2).

For $z = 1$, we find that increasing laser pulse energy barely affects the energy distributions. At most, it causes a small increase in the spectral intensity of the charge-resolved spectra. All $z = 1$ spectra exhibit a monotonically decreasing yield with increasing kinetic energy, and the distributions most probably peak below 100 eV. For the lowest multiply charged ions ($z = 2-4$), we report a clearly peaked energy distribution, with an asymmetrical widening of the spectra in the direction of higher energies with increasing laser pulse energy. Distributions of this kind are typically modeled by so-called “shifted Maxwell–Boltzmann–Coulomb (MBC) distributions,”^{18,25–27} where the

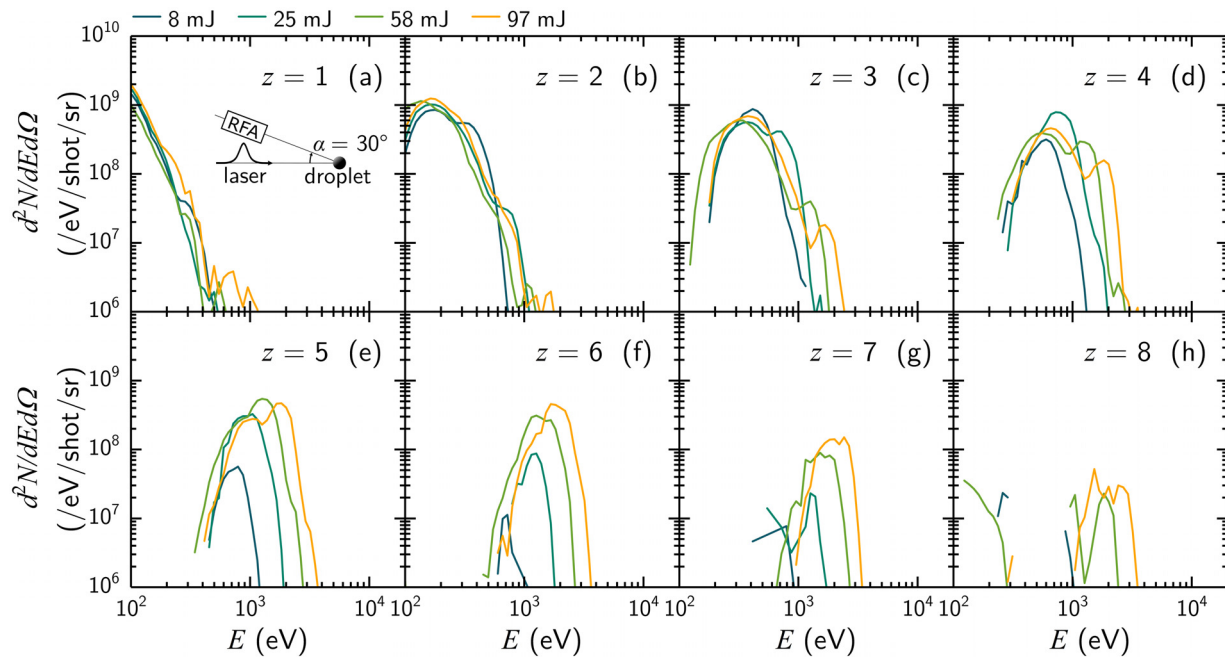


FIG. 2. (a)–(h) Charge-specific ion energy spectra for a 27- μ m-diameter droplet and four laser pulse energies ($E_L = 8, 25, 58,$ and 97 mJ), measured at 30° with respect to the direction of the laser [see the inset in panel (a)].

apparent “shifting” of these Maxwell–Boltzmann-esque distributions to high kinetic energies is attributed to (i) adiabatic expansion in the Knudsen layer^{28,29} and (ii) the formation of an accelerating voltage in the plasma that accelerates ions to energies proportional to their charge state.²⁷ A much simpler picture of ion acceleration in these plasmas is provided by quasi-neutral hydrodynamics,^{20,30} where ion acceleration (and thus the location of the peak positions) originates from gradients in the plasma pressure $\nabla p = \nabla(p_e + p_i) = \nabla[(z + 1)n_i kT]$, where $p_{e(\text{ion})}$ are the electron (ion) contributions to the pressure and z , T , and n_{ion} are the average charge state, plasma temperature, and ion density, respectively. In essence, hot and dense plasma regions generate high charge states and correspondingly high plasma pressures, spatial gradients of which form the basis for (charge-state-specific) ion acceleration.

With increasing laser energy, an additional high-energy peak emerges in the spectra. With increasing laser pulse energy, the energy corresponding to this second peak increases steadily, and its intensity decreases [Fig. 2(c)]. For higher charge states ($z > 4$), the relative spectral intensity of the second peak with respect to the first peak grows with increasing laser intensity, eventually becoming dominant with respect to the first peak. This can be seen in the spectra shown in Figs. 2(d) and 2(e), for $E_L = 97$ mJ, where the relative spectral intensities of the first and the second peak switches between $z = 4$ and 5. For a given laser pulse energy, the second peaks have the same energy for all charge states. Moreover, as charge state increases, the energy of the first peak converges to that of the second peak; they eventually merge into a single peak, for instance, for $z = 7$, in the case of the 97 mJ pulse in Fig. 2(g).

Energy spectra for $z = 1$ –8 are displayed in Fig. 3 for all seven observation angles for a 27- μm -diameter droplet illuminated by a

97 mJ laser pulse. A few immediate observations can be made. We note that at the back side ($\alpha > 90^\circ$), one collects about twice the amount of low charge states ($z = 1$ –3) as at the front side ($\alpha < 90^\circ$) for any pulse energy, while the front side generates a greater amount of high charge states ($z > 3$). Moreover, for high charge states ($z > 3$), spectra captured at small angles ($\alpha \leq 90^\circ$) peak at higher energies than those captured at large angles ($\alpha > 90^\circ$).

Next, we note that the shape of the spectra transforms with decreasing angle and increasing charge state: gradually, a shoulder appears on the high-energy side of the distributions. This effect can be seen clearly in Fig. 3(d), where the spectra peak around 600–700 eV, while a second peak feature emerges around 1.5–2 keV. The signal intensity of this second peak decreases by three orders of magnitude with increasing detection angle from 30° to 150° .

The second, high-energy peaks observed in Figs. 2 and 3 correspond to the high-energy features found in charge-integrated distributions dN/dE observed in our previous study.¹⁹ The presence of this peak was explained by a bunching phenomenon: in short, the absorption of the peak intensity of the laser pulse by the plasma generates a fast and dense expansion shell, propagating anisotropically toward small observation angles ($\alpha < 120^\circ$). This shell pushes all the slower material in its front as it expands in a vacuum, giving rise to high-energy peaks in charge-integrated spectra. Here, we find that the bunching is made up of different—relatively high—charge state ions. The absence of a second high-energy peak in dN_z/dE at large angles ($\alpha > 120^\circ$) was also observed in charge-integrated spectra.¹⁹ Additional features visible at even higher energies (around 1 keV) in Figs. 2(a), 2(b), 3(a), and 3(b) lie at noise level (here around 2×10^6 eV/shot/sr), and no significance can currently be attributed to their observation. Gaps found in the ion spectra such as the ones

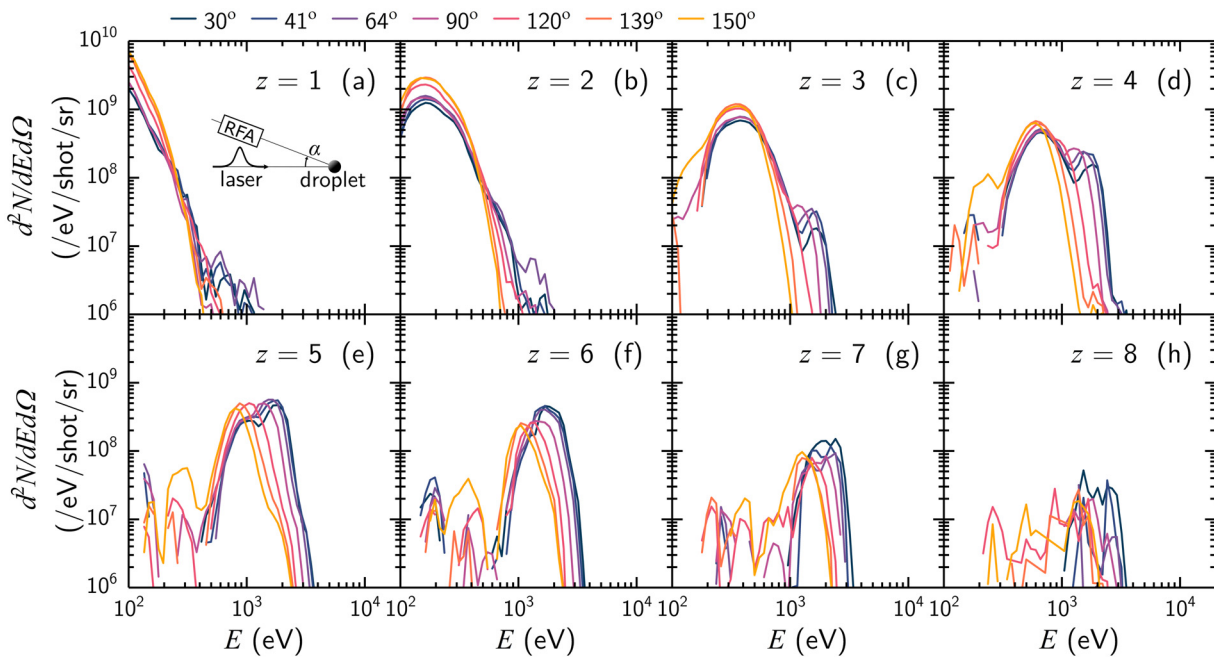


FIG. 3. (a)–(h) Charge-specific ion energy spectra measured at seven different angles with respect to the direction of the laser light propagation (30° , 41° , 64° , 90° , 120° , 139° , and 150°) for a 27- μm -diameter droplet, 97 mJ laser pulse. The inset in panel (a) defines the angle α .

observed in Fig. 2 are caused by the logarithmic representation of the y-axis, whereby negative values (originating from noise) cannot be represented.

2. Dependence of peak energies on intensity and charge state

Next, we track the energy of the maxima of the charge-state-resolved ion spectra dN_z/dE as a function of laser intensity for the 27 μm diameter and 10-ns pulse measurement. Where applicable, we track separately the first and second high-energy peaks. For $z > 4$, the two peaks merge into a single one, as seen in Fig. 3. Peak positions are recovered by (i) direct peak finding in dN_z/dE , (ii) finding roots in d^2N_z/dE^2 , and (iii) looking for minima in d^3N_z/dE^3 traces. We use a common threshold- and distance-based algorithm from the `scipy` Python library for finding peaks. The first two methods (i and ii) result in similar positions for peaked features, while the second-derivative-based method (iii) is apt for recovering the position of shoulder features. Peaks with signal intensity lower than approximately 3.5 times the local noise level are discarded in order to filter out incorrectly assigned peaks. We report the average value obtained from the three methods for the charge states $z = 2-6$ (the maximum for $z = 1$ lies out-of-range below 100 eV, and the signal intensity of $z = 7$ and 8 was insufficient for reliable application of our peak-finding methods). Figures 4(a)–4(g) show the positions of the first (full markers) and second peaks (open markers) as a function of charge state (from $z = 2$ to 6) for seven observation angles and four laser pulse intensities, for the 27- μm -diameter droplet. At all angles and laser intensities, the position of the first peak clearly increases with charge state, while that of the second peak shows a much weaker dependence on charge state.

These observations are in line with those of Kondrashev *et al.*,⁸ where the LPP target is a solid niobium plate and the 1 μm Nd-glass laser intensity is 10^{11} W/cm². We heuristically model the position of the first peak as a function of charge state as a power law $A_\alpha(z + 1)^{B_\alpha}$ [colored dashed lines in Figs. 4(a)–4(g)]. The $z + 1$ term in the model is motivated by the scaling of the plasma pressure (see above). Data points corresponding to merged first and second peaks are also used for fitting and are labeled as pertaining to the second peak category in Fig. 4; this is the case for example for the 97 mJ, $z = 6$ peak found around 1800 eV in Fig. 4(a). The recovered power-law exponents are displayed in Fig. 4(h) for each laser intensity. For the lower laser intensities, we find a nearly constant value of the power-law exponent of about 2. At higher laser intensity, we find a stronger dependence of the exponent on angle α to converge to the same value at larger angles. The error bars displayed in Fig. 4(h) correspond to the parameter’s standard deviation obtained from the power-law fit to the data. Murakami *et al.*³¹ and Mora² reported that the energy derived from the local characteristic sonic speed of the plasma E scales linearly with local temperature T and charge state z ,

$$E \propto Tz. \tag{3}$$

From the viewpoint of plasma expansion governed by radiation hydrodynamics, i.e., expansion driven mostly by plasma pressure gradients in a hot-and-dense neutral fluid, a view that is strongly supported by our previous findings,^{19,20} we may reason that the local characteristic sonic speed provides a meaningful measure of the detected ion energies. The experimentally observed scaling is not linear with charge state, hinting, taking a hydrodynamic view, that the detected ions are generated in regions of the tin plasma of different local temperatures T .

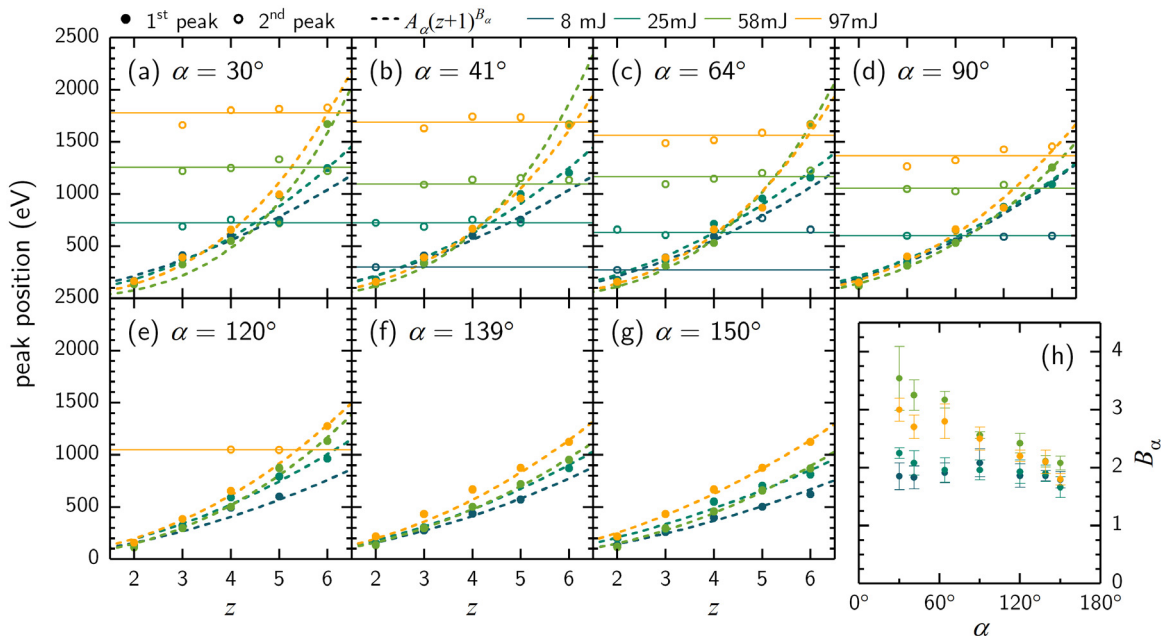


FIG. 4. (a)–(g) First (full markers) and second peak (open markers) positions in charge-state resolved spectra as a function of charge state for seven observation angles α . The horizontal lines are averages of the second peak position. Positions of the first peak are fitted with a power law $A_\alpha(z + 1)^{B_\alpha}$ [colored dashed lines in (a)–(g)], and the power-law exponents B_α are reported in panel (h); symmetrical error bars above and below the value of the exponents are defined as the statistical deviation obtained from the fit.

In addition to the strong scaling of the first peak with charge state, we observe a near-constant value of the energy of the second peak for charge states $z = 2-6$. However, this value increases strongly with increasing laser intensity. The horizontal lines in Figs. 4(a)–4(e) show the increasing average position of the second peak with increasing laser intensities.

Next, we study the laser-intensity dependence of the positions of the two peaks. In Figs. 5(a)–5(e), the same spectral maxima are shown for each charge state, now as a function of laser intensity for each of the seven angles at which ion kinetic energies were measured.

Overall, the effect of increasing the laser intensity is an increase in the first or merged peak energy. Moreover, as seen in Fig. 3, it is apparent that the first peak energy (full markers) decreases with observation angle α for all intensities and charge states. For a given pulse intensity, the peak kinetic energy increases with charge state, up to 4 or 5, at which point the first peak merges with the higher-energy second peak (open markers). In all instances of overlapping first and second peaks, there is a systematic bias in the recovery of the peak position due to the overlap of the two peaks of different amplitude and widths, referred to as line pulling. This may generate a slight overestimation of the first peak position and an underestimation of that of the second peak.

We fit power-law models ($A_z I^{B_z}$, dotted black and green lines, respectively) to the positions of the charge-resolved first and second peaks (separately) from Figs. 5(a)–5(e), and report, in the inset of Fig. 5(f), the exponents for the first peak ($B_{1,z}$) and second peak ($B_{2,z}$) for each charge state (colored markers). The values of $B_{1,z}$ and $B_{2,z}$ averaged over all available angles are calculated for each charge state and shown in Fig. 5(f) (black and green lines and triangles, respectively).

The first peak scaling exponent $B_{1,z}$ increases steadily from approximately 0 up to a value of 0.25 from $z = 2$ to 6, at which point the first peak has merged with the high-energy second peak. The scaling exponent of the second peak positions $B_{2,z}$ varies between 0.5 and 0.8, with an average value of 0.67 (green dotted line).

The scaling exponents $B_{2,z}$ for $z < 6$ take similar values; this is explained by the common bunching behavior of the underlying ions. We also expect those scaling exponents to be similar to that of the peaks found in charge-integrated spectra, which were observed in an earlier study.¹⁹ This point is specifically addressed later in Sec. III B.

We note that whereas the ion kinetic energy spectra show a very strong dependence on the emission angle, the power-law scalings extracted from the spectra show a relatively weak angular dependence. Overall, the same trends were observed in experiments with droplet targets of different diameters. We hypothesize that although the one-sided laser heating drives strong anisotropies,¹⁹ the unique link between temperature, charge state, and kinetic energy that is effectively captured in the power-law representation should indeed be independent of the observation angle under conditions of radial flow. Furthermore, study is required to more comprehensively explain the results for the individual charge states and may involve particle-in-cell (PIC) numerical modeling.

B. Intensity dependence of charge-integrated ion energy spectra

The RFA charge-integrated energy distributions dN/dE are obtained by adding up the charge-resolved energy distributions of all

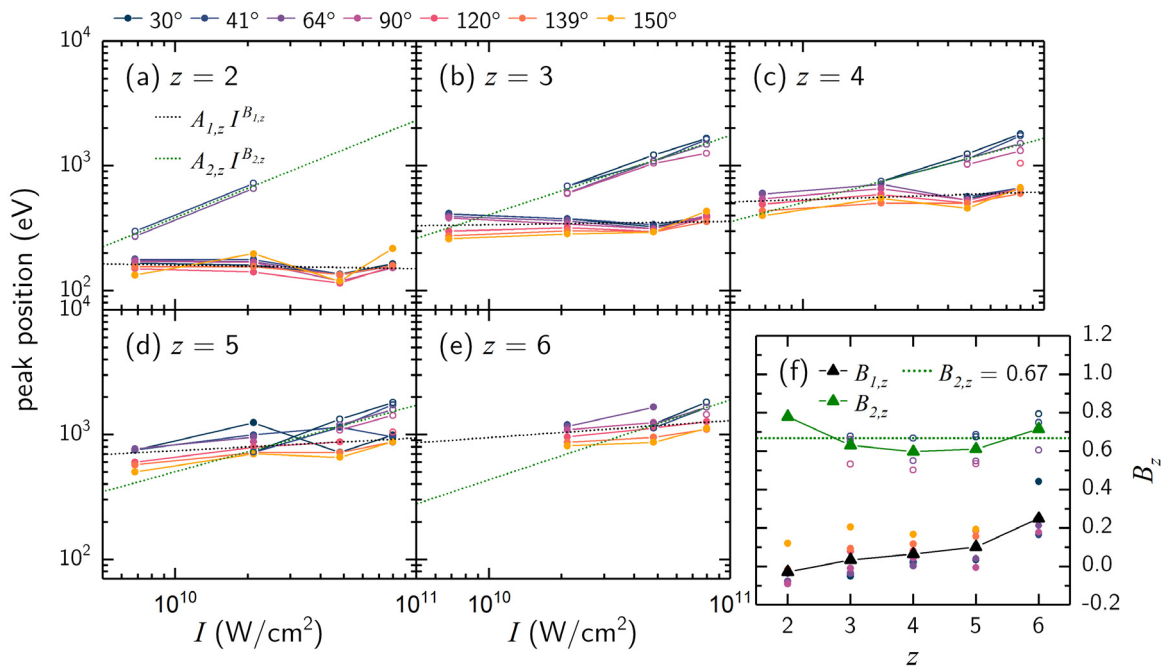


FIG. 5. (a)–(e) Positions of the first (full markers) and second (open markers) ion energy peaks, for charge states $z = 2-6$, and for seven angles α between 30° and 150° ; for each charge state, seven data sets corresponding to the seven observation angles are fitted separately with a power law; the averages of the seven fitted power laws are presented (black and green dotted lines for the first and second peaks, respectively); panel (f) shows the power-law exponents B_z [closed and open circles stand for the first and second peaks, respectively, and the color scheme follows that of (a)–(e)] as well as the exponents averaged over all available observation angles as a function of charge state z (black triangles for the first peak $B_{1,z}$ and green triangles for the second peak $B_{2,z}$). Fit results for the individual angles are also shown.

charge states present in the experiment. Those distributions are akin to, and can be readily compared with, the flow velocity distributions obtained from hydrodynamic simulations such as the ones generated by the code RALEF-2D, and give access to the momentum and energy of the plasma ions.

Figures 6(a)–6(g) show measured pulse-energy-dependent ion energy spectra for a 27- μm -diameter droplet and a 10 ns pulse duration. For ease of comparison, the spectra at minimum, medium, and maximum observation angle α are presented for the pulse energy extrema of 8 and 97 mJ in panel (h). First, we observe a spectral shift to higher energies with increasing laser energy at all angles. Second, at large angles ($\alpha \geq 90^\circ$), we note an increasing number of ions with increasing laser energy. O'Connor *et al.* presented similar findings for the front-side ($\alpha < 90^\circ$) emission using a planar target of solid tin.¹⁸ A high-energy peak is also observed in spectra with an observation angle smaller than 120° . This peak is formed by the accumulation around the same kinetic energy of ions with charge state $z \leq 4$, as seen in Sec. III A. The peak was reported,^{21,22} and its physical origin examined^{19,20} before—but only for a single laser intensity case. As the observation angle α increases, the peak loses its prominence and gradually fades into the smooth monotonously decaying background ion signal beyond $\alpha > 120^\circ$.

In the following, we look into the energy of the high-energy peak for forward emission angles ($\alpha \leq 120^\circ$) as a function of the employed laser intensity. We determine the position of the peak using a combination of direct numerical peak finding in dN/dE and looking for minima in d^2N/dE^2 (as before, the Python package `scipy` and its threshold-based peak finding routine is used here). The central peak energy shifts with laser intensity, which is shown in Figs. 7(a)–7(e) for the five relevant angles (recall that the peak is observed only for $\alpha \leq 120^\circ$), all four laser pulse energies, and all three droplet diameters of 17, 27, and 35 μm . To probe any influence of the small difference in

pulse duration (related to the Q-switch delay settings, see above), two 17 μm droplet diameter measurements are investigated, one using an 8 ns FWHM_t and the other a longer 10 ns FWHM_t laser pulse.

We observe a consistent power-law-like dependence ($A_z E^{B_z}$) of the high-energy peak position on laser intensity, with little deviation from the fitted power laws [dashed black lines in Figs. 7(a)–7(e)]. We find no significant differences between the short- and long-pulse cases for the 17- μm -diameter droplet. The exponents B_z of the power-law fits are shown in Fig. 7(f). For each of the (a)–(d) panels, we also fit power-law functions to data subsets containing three out of the four data sets to assess the fit uncertainty. For each angle α , the difference between the maximum and minimum power-law exponents thus obtained define the (systematic) error bars for B_z as shown in Fig. 7(f). In all spectra, there is a sub-linear dependence of the high-energy peak position with laser intensity, with exponents B_z ranging from 0.55 to 0.75, and an average $\bar{B}_z = 0.67(5)$, weighted by the corresponding uncertainty.

Analytical scaling relations are used to establish the dependence of characteristic LPP ion energy E with laser intensity I . In addition to Eq. (3), Basko *et al.*³² in their work on radiation hydrodynamics modeling of LPP find that

$$\bar{z} \propto T^{0.60}, \quad (4)$$

where \bar{z} is the local average charge state. Basko *et al.*³² also reported that

$$T \propto I^{0.44}, \quad (5)$$

where I is the laser intensity. Using Eqs. (3)–(5), we next derive a prediction for the typical kinetic energy as a function of laser intensity

$$E \propto T^{1+0.60} \propto (I^{0.44})^{1.60} \Rightarrow E \propto I^{0.70}. \quad (6)$$

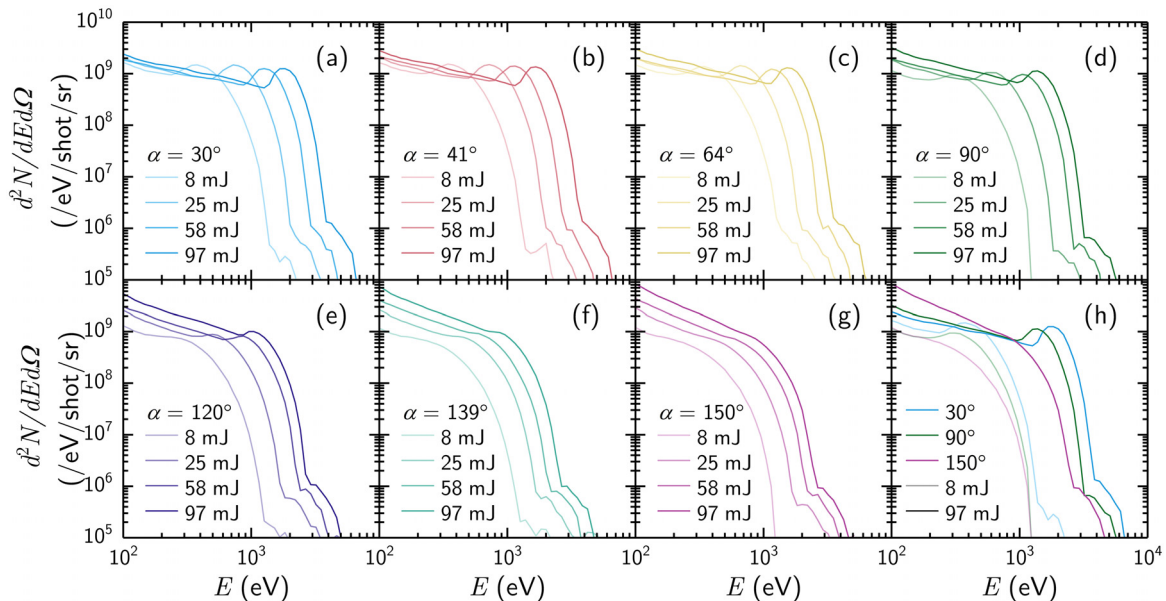


FIG. 6. Measured ion energy distributions recorded at seven angles [panels (a)–(g)], for a 27- μm -diameter droplet and four different laser intensities. For comparison, ion spectra from a small (30°), medium (90°), and large angle (120°) are reproduced in panel (h) for lowest and highest laser pulse energies ($E_{\text{pulse}} = 8$ and 97 mJ, respectively).

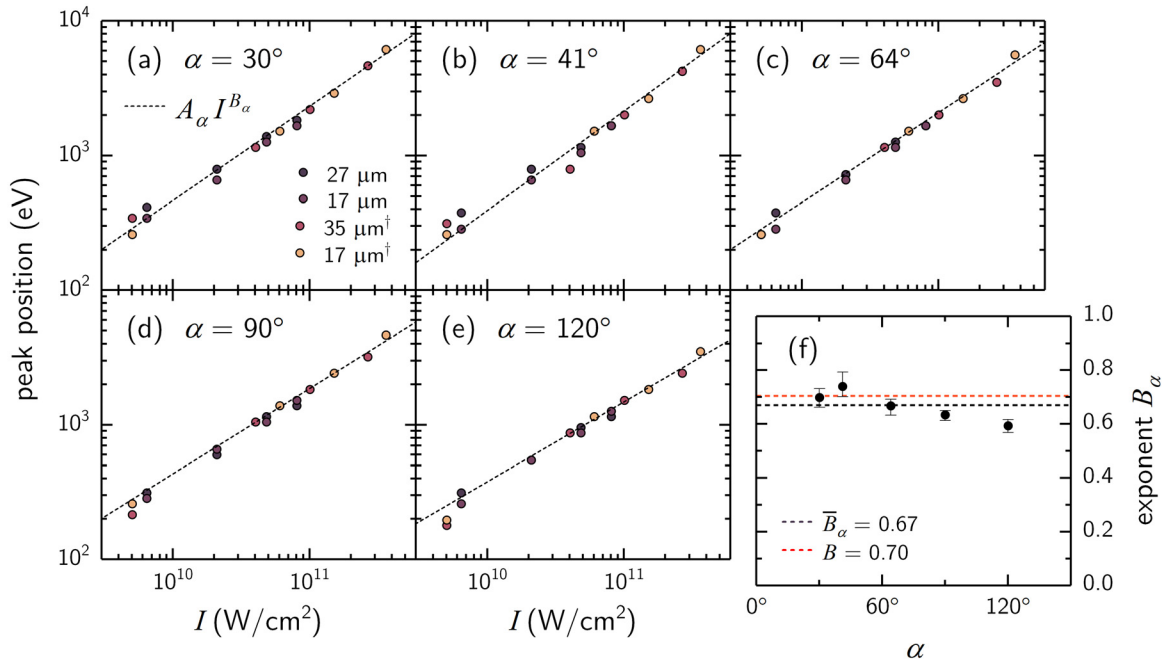


FIG. 7. (a)–(e) High-energy peak energy from calculated energy spectra (Fig. 6) as a function of laser pulse intensity for seven detection angles, three droplet diameters, and two laser pulse durations for the 17- μm -diameter case. The collective intensity dependence is optimized with a power-law scaling; panel (f) shows the exponent B_α for each angle α , their weighted average of 0.67(5) (black dashed line); the estimate [cf. Eq. (6)] of 0.70 is also shown (red dashed line).

The expected value of the power-law exponent is remarkably close to the average angle-averaged experimental values of 0.67(5) reported in Fig. 7(f), for three different droplet diameters. This finding supports the interpretation of the ionic emission from the LPP in terms of hydrodynamic plasma expansion. Moreover, the angle-averaged scaling exponent \bar{B}_z of the peak in the charge-integrated spectra matches precisely that of the second, high-energy peak in charge-resolved spectra obtained in Sec. III A. This finding corroborates the formation of the peak in dN/dE through a bunching phenomenon.

Once again, we note that despite the remarkable differences observed in spectra taken at different angles, the power-law scaling obtained by tracking features in the ion energy distribution presents a rather constant value over the angles [cf. Fig. 7(f)]. This observation holds for all studied set droplet sizes.

IV. CONCLUSION

The ion emission from tin laser-produced plasma is characterized experimentally as a function of laser pulse intensity. Energy, charge state, and emission angle of the ions are obtained using seven retarding field analyzers. Charge-resolved ion energy spectra reveal the existence of two distinct peaks in the kinetic energy distribution of individual charge states. The kinetic energy of the first peak is found to smoothly scale (superlinearly) with ion charge state, hinting—from a hydrodynamics viewpoint on the expansion process—that the detected charge states are generated at different local temperatures. The second peaks found in charge-resolved distributions dN_z/dE combine, leading to the feature in the charge-integrated energy distributions dN/dE

reported previously,^{19,20} corroborating the formation of the peak in dN/dE through a bunching phenomenon. The energy corresponding to this second, high-energy peak is found to scale at all angles with $I^{0.67(5)}$, in good agreement with empirical scaling laws derived from hydrodynamic theory of plasma expansion. This scaling relation exhibits strong isotropy, whereas the underlying ion energy spectra themselves are highly anisotropic. Our findings underpin previous interpretations^{19,20} of the peaked features in the kinetic energy distributions and, with the wide laser range of laser intensities characterized in the current work, enable predicting their energy as a function of laser intensity under conditions relevant to nanolithography light sources.

ACKNOWLEDGMENTS

The authors thank Duncan Verheijde for his support in understanding and improving the RFA electronics. They also thank Jorijn Kuster for the indispensable software support of our experimental setups. This work has been carried out at the Advanced Research Center for Nanolithography (ARCNL). ARCNL is public-private partnership with founding partners UvA, VU, NWO-I, and ASML, and associate partner RUG. This project has received funding from European Research Council (ERC) Starting Grant No. 802648. This publication is part of the project New Light for Nanolithography (with Project No. 15697) of the research program VID1, which is (partly) financed by the Dutch Research Council. This work made use of the Dutch National e-Infrastructure with the support of the SURF Cooperative using Grant No. EINF-2947.

AUTHOR DECLARATIONS

Conflict of Interest

The authors have no conflicts to disclose.

Author Contributions

Lucas Poirier: Conceptualization (equal); Data curation (equal); Formal analysis (equal); Funding acquisition (equal); Supervision (equal); Visualization (lead); Writing – original draft (lead); Writing – review & editing (equal). **Adam Lassise:** Conceptualization (equal); Methodology (equal); Writing – review & editing (equal). **Ronnie Hoekstra:** Conceptualization (equal); Supervision (equal); Writing – review & editing (equal). **John Sheil:** Conceptualization (equal); Methodology (equal); Writing – review & editing (equal). **Oscar Versolato:** Conceptualization (equal); Data curation (equal); Formal analysis (equal); Funding acquisition (equal); Supervision (equal); Visualization (lead); Writing – original draft (lead); Writing – review & editing (equal).

DATA AVAILABILITY

The data that support the findings of this study are available from the corresponding author upon reasonable request.

REFERENCES

- ¹M. Murakami and M. M. Basko, “Self-similar expansion of finite-size non-quasi-neutral plasmas into vacuum: Relation to the problem of ion acceleration,” *Phys. Plasmas* **12**(1), 012105 (2006).
- ²P. Mora, “Plasma expansion into a vacuum,” *Phys. Rev. Lett.* **90**(18), 185002 (2003).
- ³A. V. Gurevich, L. V. Pariiskaya, and L. P. Pitaevskii, “Self-similar motion of rarefied plasma,” *J. Exp. Theor. Phys.* **22**, 449 (1966).
- ⁴M. Brandstätter, N. Gambino, and R. S. Abhari, “Temporally and spatially resolved ion dynamics of droplet-based laser-produced tin plasmas in lateral expansion direction,” *J. Appl. Phys.* **123**(4), 043308 (2018).
- ⁵N. Gambino, M. Brandstätter, B. Rollinger, and R. Abhari, “A hemispherical Langmuir probe array detector for angular resolved measurements on droplet-based laser-produced plasmas,” *Rev. Sci. Instrum.* **85**(9), 093302 (2014).
- ⁶S. Fujioka, H. Nishimura, K. Nishihara, M. Murakami, Y. G. Kang, Q. Gu, K. Nagai, T. Norimatsu, N. Miyahara, Y. Izawa, K. Mima, Y. Shimada, A. Sunahara, and H. Furukawa, “Properties of ion debris emitted from laser-produced mass-limited tin plasmas for extreme ultraviolet light source applications,” *Appl. Phys. Lett.* **87**(24), 241503 (2005).
- ⁷R. A. Burdt, Y. Ueno, Y. Tao, S. Yuspeh, M. S. Tillack, and F. Najmabadi, “Recombination effects during expansion into vacuum in laser produced Sn plasma,” *Appl. Phys. Lett.* **97**(4), 041502 (2010).
- ⁸S. Kondrashev, T. Kanesue, M. Okamura, and K. Sakakibara, “Features of ion generation using Nd-glass laser,” *J. Appl. Phys.* **100**(10), 103301 (2006).
- ⁹A. Z. Giovannini, N. Gambino, B. Rollinger, and R. S. Abhari, “Angular ion species distribution in droplet-based laser-produced plasmas,” *J. Appl. Phys.* **117**(3), 033302 (2015).
- ¹⁰O. Morris, P. Hayden, P. Dunne, F. O’Reilly, G. O’Sullivan, E. L. Antonsen, S. N. Srivastava, K. C. Thompson, and D. N. Ruzic, “Determination of charge state, energy and angular distributions of tin ions emitted from laser produced plasma based EUV sources,” *J. Phys.* **58**(18), 391 (2007).
- ¹¹O. Morris, A. O’Connor, E. Sokell, and P. Dunne, “Angular distribution of the ion emission from a tin-based laser-produced plasma extreme ultraviolet source,” *Plasma Sources Sci. Technol.* **19**(2), 025007 (2010).
- ¹²P. Yeates, C. Fallon, E. T. Kennedy, and J. T. Costello, “Charge resolved electrostatic diagnostic of colliding copper laser plasma plumes,” *Phys. Plasmas* **18**(10), 103104 (2011).
- ¹³R. Kelly and R. Dreyfus, “Reconsidering the mechanisms of laser sputtering with Knudsen-layer formation taken into account,” *Nucl. Instrum. Methods Phys. Res., Sect. B* **32**(1), 341 (1988).
- ¹⁴P. Hess, R. Bailey, A. Boccara, and G. Physikzentrum, *Photoacoustic, Photothermal, and Photochemical Processes at Surfaces and in Thin Films*, Topics in Current Physics Vol. 47 (Springer-Verlag, Bad Honnef, 1989).
- ¹⁵J. C. S. Kools, T. S. Baller, S. T. De Zwart, and J. Dieleman, “Gas flow dynamics in laser ablation deposition,” *J. Appl. Phys.* **71**(9), 4547 (1992).
- ¹⁶Q. Qin, M. Zhou, and D. Mao, “Time-of-flight mass spectrometric study on UV laser ablation of silver chloride,” *Appl. Surf. Sci.* **119**(3), 321 (1997).
- ¹⁷Z. Chen, X. Wang, D. Zuo, and J. Wang, “Investigation of ion characteristics in CO₂ laser irradiating predeformed tin-droplet plasma,” *Laser Part. Beams* **34**, 552 (2016).
- ¹⁸A. O’Connor, O. Morris, and E. Sokell, “Angular and energy distribution of Sn ion debris ejected from a laser-produced plasma source, for laser power densities in the range suitable for extreme ultraviolet lithography,” *J. Appl. Phys.* **109**(7), 073301 (2011).
- ¹⁹L. Poirier, D. J. Hemminga, A. Lassise, L. Assink, O. O. Versolato, and R. Hoekstra, “Strongly anisotropic ion emission in the expansion of Nd:YAG-laser-produced plasma,” *Phys. Plasmas* **29**, 123102 (2022).
- ²⁰D. J. Hemminga, L. Poirier, M. Basko, R. Hoekstra, W. Ubachs, O. O. Versolato, and J. Sheil, “High-energy ions from Nd:YAG laser ablation of tin microdroplets: Comparison between experiment and a single-fluid hydrodynamic model,” *Plasma Sources Sci. Technol.* **30**, 105006 (2021).
- ²¹L. Poirier, A. Bayerle, A. Lassise, F. Torretti, R. Schupp, L. Behnke, Y. Mostafa, W. Ubachs, O. O. Versolato, and R. Hoekstra, “Cross-calibration of a combined electrostatic and time-of-flight analyzer for energy- and charge-state-resolved spectrometry of tin laser-produced plasma,” *Appl. Phys. B* **128**, 39 (2021).
- ²²L. Poirier, A. Lassise, Y. Mostafa, L. Behnke, N. Braaksma, L. Assink, O. Versolato, and R. Hoekstra, “Energy- and charge-state-resolved spectrometry of tin-laser-produced plasma using a retarding field analyzer,” *Appl. Phys. B* **128**, 135 (2022).
- ²³D. Kurilovich, A. L. Klein, F. Torretti, A. Lassise, R. Hoekstra, W. Ubachs, H. Gelderblom, and O. O. Versolato, “Plasma propulsion of a metallic microdroplet and its deformation upon laser impact,” *Phys. Rev. Appl.* **6**, 014018 (2016).
- ²⁴R. Schupp, L. Behnke, Z. Bouza, Z. Mazzotta, Y. Mostafa, A. Lassise, L. Poirier, J. Sheil, M. Bayraktar, W. Ubachs, R. Hoekstra, and O. O. Versolato, “Characterization of angularly resolved EUV emission from 2- μ m-wavelength laser-driven Sn plasmas using preformed liquid disk targets,” *J. Phys. D* **54**(36), 365103 (2021).
- ²⁵L. Torrisi, S. Gammino, L. Andò, and L. Laska, “Tantalum ions produced by 1064 nm pulsed laser irradiation,” *J. Appl. Phys.* **91**(7), 4685 (2002).
- ²⁶X. Wang, S. Zhang, X. Cheng, E. Zhu, W. Hang, and B. Huang, “Ion kinetic energy distributions in laser-induced plasma,” *Spectrochim. Acta, Part B* **99**, 101 (2014).
- ²⁷F. Gobet, M. Comet, J. R. Marquès, V. Méot, X. Raymond, M. Versteegen, J. L. Henares, and O. Morice, “Signatures of fluid and kinetic properties in the energy distributions of multicharged ta ions from nanosecond-laser-heated plasma,” *Phys. Rev. E* **98**, 063202 (2018).
- ²⁸D. Sibold and H. M. Urbassek, “Kinetic study of pulsed desorption flows into vacuum,” *Phys. Rev. A* **43**, 6722 (1991).
- ²⁹R. Kelly, “Gas dynamics of the pulsed emission of a perfect gas with applications to laser sputtering and to nozzle expansion,” *Phys. Rev. A* **46**, 860 (1992).
- ³⁰R. P. Drake, *High-Energy-Density Physics*, 2nd ed. (Springer, Cham, 2018), Vol. 149.
- ³¹M. Murakami, Y. G. Kang, K. Nishihara, S. Fujioka, and H. Nishimura, “Ion energy spectrum of expanding laser-plasma with limited mass,” *Phys. Plasmas* **12**(6), 062706 (2005).
- ³²M. M. Basko, V. G. Novikov, and A. S. Grushin, “On the structure of quasi-stationary laser ablation fronts in strongly radiating plasmas,” *Phys. Plasmas* **22**(5), 053111 (2015).